PNAS RESEARCH ARTICLE | CHEMISTRY

An analytical model of label-free nanoscale chemical imaging reveals avenues toward improved spatial resolution and sensitivity

Yide Zhang[a,b], Ufuk Yilmaz[a], Gustavo Vinicius Bassi Lukasievicz[c], Liam O'Faolain[b], Bernhard Lendl[a], and Georg Ramer[a,d,1]

Affiliations are included on p. 10.

Edited by Catherine Murphy, University of Illinois at Urbana-Champaign, Urbana, IL; received February 13, 2024; accepted December 3, 2024

Atomic force microscopy–infrared spectroscopy (AFM-IR) is a photothermal scanning probe technique that combines nanoscale spatial resolution with the chemical analysis capability of mid-infrared spectroscopy. Using this hybrid technique, chemical identification down to the single molecule level has been demonstrated. However, the mechanism at the heart of AFM-IR, the transduction of local photothermal heating to cantilever deflection, is still not fully understood. Existing physical models only describe this process in few special cases but not in many of the types of sample geometries encountered in the practical use of AFM-IR. In this work, an analytical expression for modeling the temperature and photothermal expansion process is introduced, verified with finite element simulations, and validated with AFM-IR experiments. This method describes AFM-IR signal amplitudes in vertically and laterally heterogeneous samples and allows studying the effect of position and size of an absorber, pump laser repetition rate and pulse width on AFM-IR signal amplitudes and spatial resolution. The analytical model can be used to identify optimal AFM-IR experimental settings in conventional and advanced AFM-IR modes (e.g., tapping mode, surface-sensitive mode). The model also paves the way for signal inversion based superresolution AFM-IR.

atomic force microscopy–infrared | nanoscale chemical imaging | analytical model | photothermal expansion

Significance

Atomic force microscopy–infrared spectroscopy (AFM-IR) is a widely used scanning probe technique for label-free photothermal nanoscale chemical imaging, with diverse applications spanning single protein spectroscopy to analyzing nanoscale chemical, physical, and optical phenomena. However, the understanding of spatial resolution of the technique is limited to few specific, simple geometries (spheres, pillars, etc.). We introduce an analytical model of AFM-IR verified by numerical simulations and experiments that describes experimental data well for complex sample geometries. The model allows to reason about the spatial resolution and sensitivity of the technique and can give guidance for optimizing experimental parameter for sensitivity and resolution and interpreting results. Beyond this, it can be a stepping stone toward superresolution AFM-IR or nanoscale chemical tomography.

Atomic force microscopy–infrared spectroscopy (AFM-IR) is a near-field technique combining atomic force microscopy (AFM) and mid-infrared (IR) spectroscopy, which achieves nanoscale spatial resolution optical imaging independent of the wavelength (1–3) and thus enables chemical analysis based on infrared spectroscopy orders if magnitude below the diffraction limit (4–8).

A typical AFM-IR setup consists of a pulsed laser focused onto a sample at the location of the tip of an AFM cantilever (Fig. 1*A*). In general, the working principle of this technique (2, 9) is described by focusing on the change of the sample's density, which induces a localized sample expansion. The partial or total absorption of light from the pulsed laser by molecules distributed in the sample results in a local temperature increase affecting the density and refractive index of the sample at the place of absorption. A train of laser pulses will thus generate a modulated temperature change in the sample leading to photothermal and photoacoustic waves that propagate within the sample. AFM-IR employs the spatially resolved detection of the photothermal expansion of the sample by the AFM's cantilever upon illumination with a pulsed light source (Fig. 1*B*).

Absorption of light from the laser pulse leads to local temperature increase and concurrent thermal expansion (Fig. 1*C*). As the heat is redistributed within the sample this local expansion subsides.

Using a laser with adjustable pulse repetition rate, the mechanical resonances of the cantilever can selectively be excited (10) when the laser repetition rate matches the selected mode of the cantilever. In this scenario, the photothermal expansion stimulates the AFM cantilever at its oscillation's resonance frequency (Fig. 1*D*), hereby selectively amplifying the AFM-IR signal which can be demodulated from the AFM deflection signal.

This general working principle is well accepted in the community and the ability of AFM-IR for chemical imaging is well established, with applications ranging from materials (11, 12) to biological samples (6, 13, 14) and photonics, perovskites (15), and semiconductors (2, 16). Several groups have studied the AFM-IR imaging contrast mechanism. The initial theoretical description of AFM-IR signal generation and transduction was established by Dazzi et al. (17, 18), who considered a homogeneous

Author contributions: G.R. designed research; Y.Z. and U.Y. performed research; Y.Z. and G.R. analyzed data; and Y.Z., U.Y., G.V.B.L., L.O., B.L., and G.R. wrote the paper.

The authors declare no competing interest.

This article is a PNAS Direct Submission.

[1]To whom correspondence may be addressed. Email: georg.ramer@tuwien.ac.at.

This article contains supporting information online at https://www.pnas.org/lookup/suppl/doi:10.1073/pnas.2403079122/-/DCSupplemental.

Published January 24, 2025.

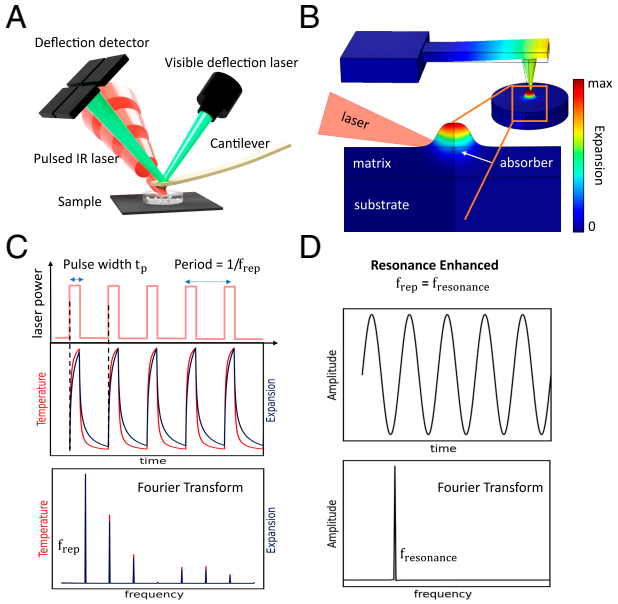

Fig. 1. Schematic illustration of the resonance enhanced AFM-IR. (*A*) Sketch illustrating the AFM-IR setup. The sample is placed on a piece of silicon (gray) and illuminated from the top with a pulsed, tunable, infrared beam (red). (*B*) The sample location that absorbs the energy of IR laser which is then transformed into temperature change and thermal expansion. The sample's photothermal expansion excites the cantilever into oscillations. (*C*) In the excitation process, temperature and expansion increase during the pulse time (t_p) and repeat the same process with the repetition frequency (f_{rep}). The signal in frequency domain will only present at the f_{rep} and its higher-order modes. While operating AFM-IR at contact mode, in the resonance-enhanced operation (*D*), f_{rep} matches the selected resonance frequency of the cantilever to resonantly exciting it, thereafter, the enhanced AFM-IR signal is proportional to the mode's quality factor.

sample without accounting for geometry, illuminated with single pulse laser. While this model does not describe the spatial resolution of AFM-IR, it shows that the thermal expansion is linearly proportional to the local absorption.

Later, Morozovska et al. studied the contrast formation mechanism of T-shape boundary between two materials in nanoscale IR spectroscopy (19). In this model, using two semi-infinite materials with an interface orthogonal to the AFM scanning plane, temperature distribution and mechanical displacement of both absorber and the neighboring material is described, taking into account various factors, including different IR-radiation absorption coefficients and thermo-physical and elastic properties of the two materials. These properties encompass thermal diffusivities, thermal conductivities, and elastic stiffness, as well as thermal expansion coefficients. This model indicates higher modulation frequency would provide a significantly higher spatial resolution. Schwartz et al. (20) devised an analytical model to depict the photothermal expansion of a homogenous sample, factoring in a single laser pulse. They considered the laser heating profile and performed numerical simulations on heterogeneous samples comprising two adjacent materials. This study aimed to elucidate the dependence of signal transduction efficiency and spatial resolution on laser pulse width, pulse shape, sample thermalization time, and interfacial thermal resistance, etc., and found this model in good agreement with their previous experimental investigations (21, 22).

However, in many cases, AFM-IR samples do not conform to the geometries described in literature. Particularly, many samples consist of absorbers embedded within a larger matrix, such as inclusion bodies inside a cell (23), metal soaps in paint layers (24) or even organelles (25).

Interpreting AFM-IR signals poses a challenge due to sample heterogeneity. This challenge—often overlooked—requires deconvolution of the signal generation from sample contributions. Our study addresses this crucial aspect, emphasizing its significance not only for AFM-IR but also for scanning probe techniques in a more broad sense.

In the present work, we develop a model describing the whole AFM-IR signal generation process, starting with light absorption by an absorber embedded in a matrix until detection of the sample's surface expansion. This model takes into account thermal and mechanical properties of materials, as well as the size and position of the absorber. The vertically and laterally inhomogeneous sample comprising an analyte embedded in a matrix is relevant to a wide range of common AFM-IR applications such as the detection of organelles within a cell (26) or contamination within a polymer layer (27).

Our approach uses an analytical description of the time-dependent heating and sample deformation based on Green's functions. This model is a better match to real-world problems encountered in the life and material sciences than previously described analytical models, such as lumped linear proportional models. It provides exact mathematical expressions for the variables of interest, yielding clear insights into their relationships in an easily interpretable form. While models based on finite element modeling (FEM) are able to incorporate more details, here, our approach excels in computational efficiency.

This Green's function approach, whereby the response of a system to an excitation is determined by convolving the distribution of the absorbers and the time domain shape of the pump laser pulse with a system response function has some interesting parallels to signal processing and optical microscopy: Along the temporal axis, the sample can be understood to act as a low pass filter upon the excitation pulse shape and in the spatial dimension, our model exhibits similarities to a point spread function (PSF) that is typically used to understand and characterize spatial resolution in optical imaging. Thus, this "PSF model of AFM-IR" enables us to directly compare the spatial resolution in optical imaging techniques and with those achieved in AFM-IR. Furthermore, it allows the efficient modeling of the response of samples with arbitrary absorber distribution.

To arrive at a PSF model of AFM-IR that can be algebraically handled, certain assumptions regarding the sample geometry and properties need to be made. To ensure the validity of these assumptions, we compare the PSF model to finite element simulations which we can validate against experimental AFM-IR data. Through this validation process, we observe a strong agreement between the PSF model of AFM-IR, finite element simulations, and experimental results.

With the validated PSF model of AFM-IR, we are able to make general predictions regarding the spatial resolution and signal intensity in AFM-IR. Specifically, we can investigate how these parameters are influenced by factors such as the pulse width and repetition rate of the excitation laser, as well as the thermal and mechanical properties of the sample. By leveraging the PSF model, we gain valuable insights into the fundamental aspects of AFM-IR and its performance characteristics.

We show that this model will help to understand how experimental parameters (pulse rate, pulse width, sample stiffness, sample geometry,...) influence the performance of advanced AFM-IR techniques, such as tapping mode AFM-IR (28), or the recently introduced surface-sensitive AFM-IR (29).

Results and Discussion

Modeling the AFM-IR Signal. In laterally homogeneous samples, the surface expansion is proportional to the temperature change of the sample after a laser pulse, hence for such samples the signal can fairly accurately be described if only sample heating and thermal conduction are taken into account (7). However, to study spatial resolution in AFM-IR, models that describe laterally heterogeneous samples are required. Here, surface displacement also depends on the elastic response of the sample (19), as the inhomogeneous, absorber distribution–dependent heating and creates inhomogeneous strain in the neighboring material. There are three components in our description of AFM-IR: transient laser heating of the sample, heat conduction within the sample, and thermo-elastic deformation of the sample.

More specifically, laser heating is described as a time-dependent volumetric heat source $g(\mathbf{x}, t)$, where $\mathbf{x}$ represents any location in the domain. Thermal conduction is described by Fourier's law

$$\nabla^2 T(\mathbf{x}, t) + \frac{1}{\kappa} g(\mathbf{x}, t) = \frac{1}{\alpha} \frac{\partial T(\mathbf{x}, t)}{\partial t}, \qquad [1]$$

where κ is the thermal conductivity and α is the thermal diffusivity. In the equilibrium state, thermo-elastic sample deformation without external force is described by Navier's equations of thermoelasticity (30),

$$\mu \nabla^2 \mathbf{u}_i + (\lambda + \mu) \frac{\partial e}{\partial \mathbf{x}_i} - \beta \frac{\partial T(\mathbf{x}, t)}{\partial \mathbf{x}_i} = 0, \qquad [2]$$

where e is dilatation, $i \in \{1, 2, 3\}$ are indices of Cartesian coordinates, λ and μ are the Lamé elastic constants, and β is the thermo-elastic constant. The AFM-IR signal is proportional to the surface displacement. Depending on the type of transducer, either the amplitude of displacement at a specific frequency (4) or the time-dependent surface displacement (10) is recorded in AFM-IR. Considering the insignificance of the photoacoustic signal in AFM-IR measurements compared to the photothermal signal, along with its tendency to introduce artifacts (29), we have made the decision not to include it in the current model.

Assuming the system is in thermal equilibrium before excitation with a laser pulse, its response is determined through convolution of $g(\mathbf{x}', t)$ with a Green's function $G(\mathbf{x}, t|\mathbf{x}', t')$. Green's function represents the temperature at any location $\mathbf{x}$ within the domain, at any time t, due to an instantaneous volumetric source, located at the position $\mathbf{x}'$, releasing its energy spontaneously at time $t = t'$ into a medium at steady-state conditions. To find G and solve Eqs. **1** and **2**, we use assumptions that have been previously shown to describe the thermal behavior of AFM-IR experiments well (7): 1) the sample is a homogeneous material of known thickness that is 2) placed on a substrate acting as a heat sink and 3) covered by an insulating layer (air) (Fig. 2*A*).

In the following sections, we will first develop the analytical model, then verify that our model does not give significantly different results from a model that uses finite thermal conductivities for the cover layer and the substrate, by comparing the results from the analytical model with those calculated using a FEM.

Model results are additionally compared to experimental AFM-IR data of a polymethyl methacrylate (PMMA) absorber embedded in a polyethylene (PE) matrix. In *Results and Discussion*, we intend to present predictions regarding the resolution and signal intensity dependencies on the depth positions of the absorber, its size, and the repetition rates of the laser.

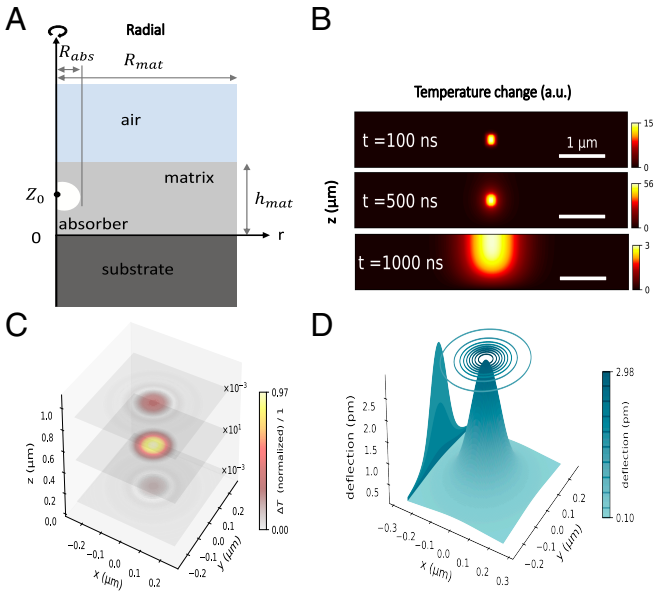

Fig. 2. Using the PSF model to describe the AFM-IR signal: (*A*) Schematic of the modeled, cylindrically symmetric system composed of a single spherical absorber surrounded by a matrix, deposited on a nonabsorbing substrate. (*B*) Lateral and vertical temperature change at different times during and after illumination with 500 ns length laser pulse. (Absorber position at $z_0 = 0.5$ µm). (*C*) Amplitude of temperature change at several depths in the sample. (*D*) Amplitude of thermo-elastic displacement at the surface. At 500 kHz and a pulse width of 500 ns.

The FEM simulations take into account additional factors, heat transfer between different materials, temperature distribution, thermal expansion in equilibrium states, and interfacial thermal conductance in agreement with other work (9, 20, 31). For AFM-IR experiments, we prepared samples with PMMA beads embedded in PE matrix, and performed a series measurements with different laser pulse widths and repetition rates.

A Green's Function Solution Describing the AFM-IR Signal. We choose a cylindrical coordinate system, for two reasons: In analogy to PSFs, it allows an axisymmetric, quasi-2D representation that is more illustrative than a three-dimensional one, without loss of generality, and has significantly lower computational cost for FEM, required for comparison.

The heat equation in cylindrical coordinates reads

$$\frac{\partial^2 T(r, z, t)}{\partial r^2} + \frac{1}{r} \frac{\partial T(r, z, t)}{\partial r} + \frac{\partial^2 T(r, z, t)}{\partial z^2} + \frac{g(r, z, t)}{\kappa} = \frac{1}{\alpha} \frac{\partial T(r, z, t)}{\partial t} \qquad [3]$$

using a finite, axisymmetric cylindrical sample of radius R_{mat} and height h_{mat}. Using the boundary conditions as outlined in the previous section, the canonical Green's function solution (32) is

$$T(r, z, t) = \frac{\alpha}{\kappa} \int_{t'=0}^{t} \int_{z'=0}^{h_{\text{mat}}} \int_{r'=0}^{R_{\text{mat}}} G(r, z, t|r', z', t') \times g(r', z', t') r' \, dr' \, dz' \, dt' \qquad [4]$$

with a Green's function

$$G(r, z, t|r', z', t') = \sum_{n=0}^{\infty} \sum_{m=0}^{\infty} \frac{4 J_0(\beta_m r) \sin(\eta_n z)}{h_{\text{mat}} R_{\text{mat}}^2 J_1^2(\beta_m R_{\text{mat}})} \times J_0(\beta_m r') \sin(\eta_n z') e^{-\alpha \lambda_{nm}^2 (t - t')}, \qquad [5]$$

where β_m, η_n and λ_{mn} are eigenvalues obtained according to boundary conditions (*SI Appendix*, section S1). While G contains an infinite sum of modes, the decay time of each mode is $1/\alpha\lambda_{mn}^2$, which decreases as integer values m and n increase. Hence, the sum can be truncated once sufficiently short time scales have been reached.

The overall sample deformation in AFM-IR is on the order of picometers (7) and experimental parameters are chosen to not change sample properties (e.g. not to cause phase transitions or damage to the sample) during the experiment. Hence, we can split the time-dependent, volumetric heat source into a spatial and a temporal component $g(\mathbf{x}, t) = g_V(\mathbf{x})g_t(t)$. The time domain variation in the illumination intensity is described by $g_t(t)$, while $g_V(\mathbf{x})$ describes the location and intensity of heating, i.e., location and magnitude of light absorption inside the sample [in the following discussion, we neglect optical effects such as interference upon the signal. These effects can be added by multiplying the absorption coefficient with the local light intensity to arrive at a modified g_V (32)]. Splitting $g(\mathbf{x}, t)$ allows us to also split the convolution in Eq. **5** into two parts, one that describes the mode amplitude and shape in r and z, and one that describes the time domain behavior of each mode:

$$T(r, z, t) = \sum_{n=0}^{\infty}\sum_{m=0}^{\infty} A(\beta_m, \eta_n)\underbrace{J_0(\beta_m r)\sin(\eta_n z)}_{\text{spatial}}\underbrace{\mathcal{T}_{nm}(t)}_{\text{temporal}}, \quad [6]$$

where $A(\beta_m, \eta_n)$ depends on the correlation between $g_V(r, z)$ and $J_0(\beta_m r)\sin(\eta_n z)$ and

$$\mathcal{T}_{nm}(t) = \int_{t'=0}^{t} g_t(t')e^{-\alpha\lambda_{mn}^2(t-t')}dt' \quad [7]$$

i.e. the convolution of $g_t(t)$ and $e^{-\alpha\lambda_{nm}^2 t}$. $g_V(r, z)$ is the product of the optical absorption coefficient and the optical fluence, as defined in *SI Appendix*, Eq. **S2**. By utilizing Eq. **6**, we can generate spatial temperature distributions within the absorber and matrix at various time points (Fig. 2*B*). In frequency domain $\mathcal{T}$ is the product of the Fourier transforms of $g_t(t)$ and $e^{-\alpha\lambda_{nm}^2 t}$, allowing an easy way to study location-dependent amplitudes of temperature changes (Fig. 2*C*).

Once $T(r, z, t)$ is known, following Noda et al.(30), the vertical sample displacement u_z at the surface can be determined from Navier's equations for axisymmetric thermoelastic problems in cylindrical coordinates as (*SI Appendix*, section S2):

$$u_z(r, h_{\text{mat}}, t) = 2(1+v)\alpha_z\sum_{n=0}^{\infty}\sum_{m=0}^{\infty}\frac{A(\beta_m, \eta_n)}{\beta_m} \times \left(\frac{\eta_n^2}{\beta_m^2+\eta_n^2}+1\right)\underbrace{J_0(\beta_m r)}_{\text{spatial}}\underbrace{\mathcal{T}_{nm}(t)}_{\text{temporal}}, \quad [8]$$

where K is the restraint coefficient (*SI Appendix*, Eq. **S39**), α_z is the coefficient of thermal expansion and

$$A(\beta_m, \eta_n) = \frac{4}{\kappa h_{\text{mat}} R_{\text{mat}}^2}\frac{\iint_V r' J_0(\beta_m r')\sin(\eta_n z')g(r', z')dr'dz'}{J_1^2(\beta_m R_{\text{mat}})\lambda_{nm}^2} \quad [9]$$

for a sphere, it is

$$A(\beta_m, \eta_n) = \frac{8R_{\text{abs}}g_V}{\kappa h_{\text{mat}} R_{\text{mat}}^2}\frac{J_1(\beta_m R_{\text{abs}})\sin(\eta_n z_0)\sin(\eta_n R_{\text{abs}})}{J_1^2(\beta_m R_{\text{mat}})\lambda_{nm}^2\beta_m\eta_n} \quad [10]$$

Again, time domain and spatial domain behavior separated in Eq. **8**.

Here, R_{abs} is the radius of the absorber. Eq. **8** provides us with ability to represent the surface displacement either in the time domain or the frequency domain. This is illustrated in Fig. 2*D* as an example.

Comparison PSF Model and FEM. To verify that the assumptions taken for the PSF model did not affect its ability to describe an actual AFM-IR experiment, the integrated temperature and surface displacement profiles calculated by the model were compared with those calculated using a FEM model of a spherical absorber consisting of PMMA embedded into a PE matrix placed on a silicon substrate. The displacement profiles conformed well to reality: Spherical absorber and matrix were assigned literature values for thermal and mechanical properties of PMMA and PE, respectively. The substrate was not set to be a perfect heat sink but a Si layer (5 µm) and instead of an insulating boundary at the cover layer, here heat transduction through thermal diffusion in air (5 µm) was modeled. The material properties for simulations are listed in *SI Appendix*, Table S1. Unless stated otherwise, the following parameters remain constant in simulations involving the FEM and PSF models of AFM-IR: $R_{\text{abs}} = 70$ nm, matrix thickness $h_{\text{mat}} = 1$ µm, the matrix radius is $R_{\text{mat}} = 5$ µm (see Fig. 2*A* for a sketch of the sample geometry).

Both models yield virtually identical integrated temperatures for all tested pulse widths (see Fig. 3*A* for the variation of integrated temperature at pulse widths of 100 ns, 300 ns, and 500 ns). Both models also agree well when it comes to the dependence of surface displacement on pulse width (Fig. 3*B*).

However, there are deviations between the Green's function model and the FEM model when using substrates (such as SiO_2) that do not act similar to a perfect heat sink for the polymer sample (*SI Appendix*, Fig. S18). It should be noted that SiO_2 is not a common substrate for AFM-IR due to its strong infrared absorption. The effects of interfacial thermal resistance and thermal conductivity of the substrate are reduced at higher

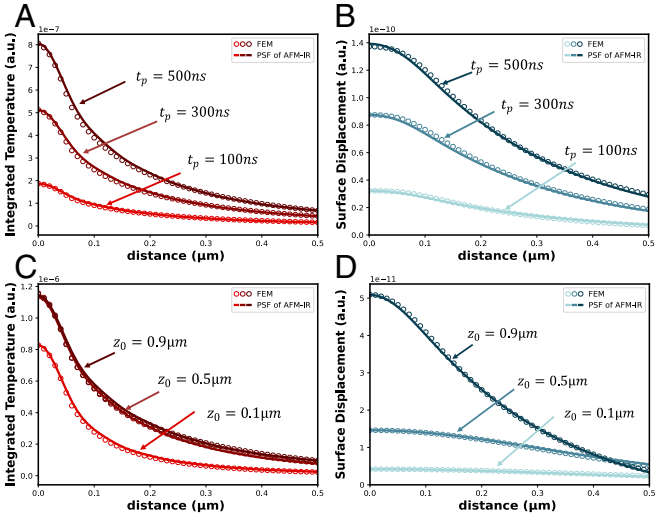

Fig. 3. Integrated temperature and displacement profile for three different laser pulse widths and depth positions of the absorber. (*A*) Temperature profile and (*B*) thermo-elastic displacement profile are examined for three different pulse widths at a laser repetition rate of 500 kHz. The absorber is positioned at a depth of $z_0 = 0.9$ µm. (*C*) Temperature profile and (*D*) thermo-elastic displacement profile are examined for three different depth positions of the absorber. At a laser repetition rate of 500 kHz and a pulse width of 100 ns.

laser repetition rates and for absorbers far from the substrate (*SI Appendix*, Fig. S19). "Far" in this case can be understood in terms of the thermal diffusion length $\mu = \sqrt{\frac{\alpha}{\pi f}}$. This result matches studies on thermal behavior of thin films (33). In case of very thin films, modifications to the Green's function model are required. However, in such samples models that assume vertical homogeneity might be more adept, such as those by Schwartz et al. (20), Morozovska et al. (19) or Dazzi's original study of the AFM-IR signal (34).

Both integrated temperature and surface displacement increase with increasing pulse width. However, it is evident that the surface displacement profile is much broader than the temperature profile. These results confirm that the thermo-elastic displacement has a nonlinear relationship with the temperature variation due to the presence of an inhomogeneous distribution of the heat source, which induces nonuniform strains in adjacent materials.

Furthermore, both models reveal distinct dependencies of integrated temperature and surface displacement on the absorber position (Fig. 3 *C* and *D*). Evidently, when the absorber is positioned closer to the surface, the surface displacement exhibits higher amplitude and a narrower profile, while the shape of the integrated temperature profile mainly depends on how quickly the heat can diffuse away from the absorber (i.e. it is narrower closer to the substrate). Likewise, a comparable dependency is evident in the surface temperature profiles (*SI Appendix*, Fig. S1).

Despite the PSF model of AFM-IR being designed for scenarios where the absorber is fully beneath the surface, we used the FEM model to understand how an absorber that extends partially beyond the surface would behave in AFM-IR. Surprisingly, we observed minimal difference in the displacement profile and amplitude for a bead that is just below the surface and one that is half below and half above the surface, as depicted in *SI Appendix*, Fig. S2. In general there is a high level of agreement between the PSF model of AFM-IR and the FEM simulations, with a mean percentage difference between both models for integrated temperature and displacement data below 3% for all tested pulse widths and depth positions of the absorber (*SI Appendix*, Fig. S3), meaning that the simplifications of the PSF model do not noticeably affect its accuracy.

The same agreement was found when other experimental parameters were adjusted, such as sample size R_{abs}, specific heat capacity C_p and thermal conductivity κ (*SI Appendix*, Fig. S4). These results indicate that the surface displacement magnitude is roughly in proportion to the absorber's volume (*SI Appendix*, Fig. S4*A*), while the full width at half maximum (FWHM) of the displacement profile does not show a proportional increase with the absorber's size (*SI Appendix*, Fig. S4*B*). Moreover, the physical properties of the matrix material play a crucial role in the signal intensity and the spatial resolution (given by the shape of the surface displacement). A matrix material with low heat capacity and thermal conductivity leads to higher signal intensity at the surface (*SI Appendix*, Fig. S4 *C* and *E*). This occurs due to the rapid heating characteristic of a material with low specific heat capacity, coupled with its limited thermal conductivity that impedes efficient heat conduction. Consequently, heat is redistributed from the absorber into the matrix material more slowly, resulting in a higher temperature and corresponding higher thermal expansion. On the other hand, a matrix material with high specific heat capacity and low thermal conductivity shows narrower surface displacement profiles. The increased heat capacity facilitates superior thermal confinement, reducing the spread of heat and enhancing the spatial resolution of the imaging (*SI Appendix*, Fig. S4*D*). Additionally, the low thermal conductivity helps to minimize heat dissipation, further enhancing the resolution of AFM-IR imaging (*SI Appendix*, Fig. S4*F*).

Comparison of Model and Experiment. A sample resembling the simulated structure using FEM and PSF model was prepared using PMMA beads with diameters of approximately 140 nm. These beads were suspended in a PE matrix and subsequently microtomed into thin slices with a thickness of 1 µm (refer to *Materials and Methods* for more details). The buried absorber (Fig. 4*A*) was detected using the 1,730 cm^{-1} carbonyl band of PMMA (Fig. 4*B*) which can be clearly distinguished from the matrix spectrum. The AFM-IR absorption image (also referred to as "chemical image") at 1,730 cm^{-1} shows a single PMMA bead (Fig. 4*C*) with a FWHM determined from the cross-section through the chemical image of 121 nm.

Here, we find another utility of the FEM based model, namely that it also allows us to model the heat flow across the interface between PMMA and PE, such as interfacial roughness, compositional disorder, or general interfacial thermal resistance (ITR) (35, 36) which could affect the thermal diffusion and thus the AFM-IR signal. To address these potential effects, we incorporated ITR between PMMA and PE ($R_{PMMA/PE}$) into the finite element simulations. However, to the best of our knowledge, no literature values exist for $R_{PMMA/PE}$ and ITR values are generally associated with high uncertainties (37, 38). Our approach consisted of utilizing reported ITR values of polymers in the model, such as the ITR in BN@PEI/PVA (2.15×10^{-6} m^2 KW^{-1}) and in BN/PVA (3.03×10^{-6} m^2 KW^{-1}) (39). Thus, by choosing the ITR in a range between the two reported values described before, and in accordance with our FEM simulations, we found that our selected value has a good agreement with experimental results (Fig. 5). These values are comparable to those used by others to simulate AFM-IR experiments (20).

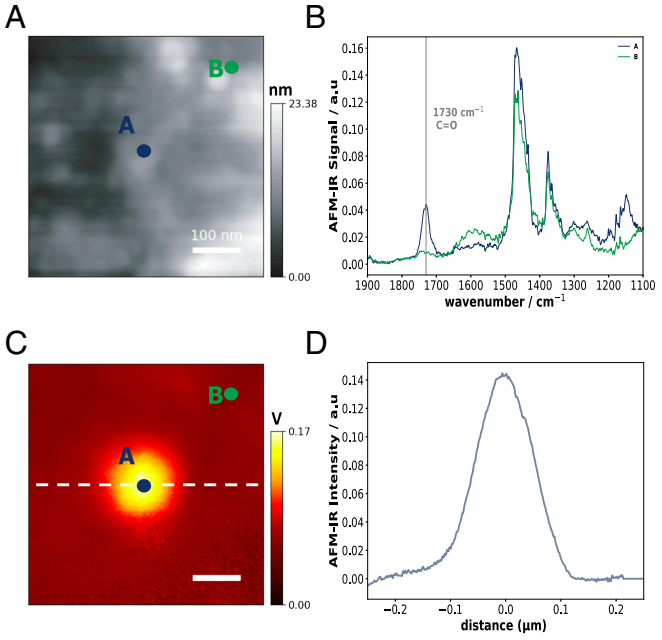

Fig. 4. PMMA bead measurement with laser repetition rate 508 kHz, pulse width 200 ns. (*A*) AFM topography image of a PMMA nanoparticle. (*B*) AFM-IR spectra obtained on positions A and B, respectively. (*C*) Corresponding AFM-IR chemical map at 1,730 cm^{-1}. The dashed line corresponds to the profile in (*D*). (*D*) Cross-section profile of the AFM-IR signal distribution.

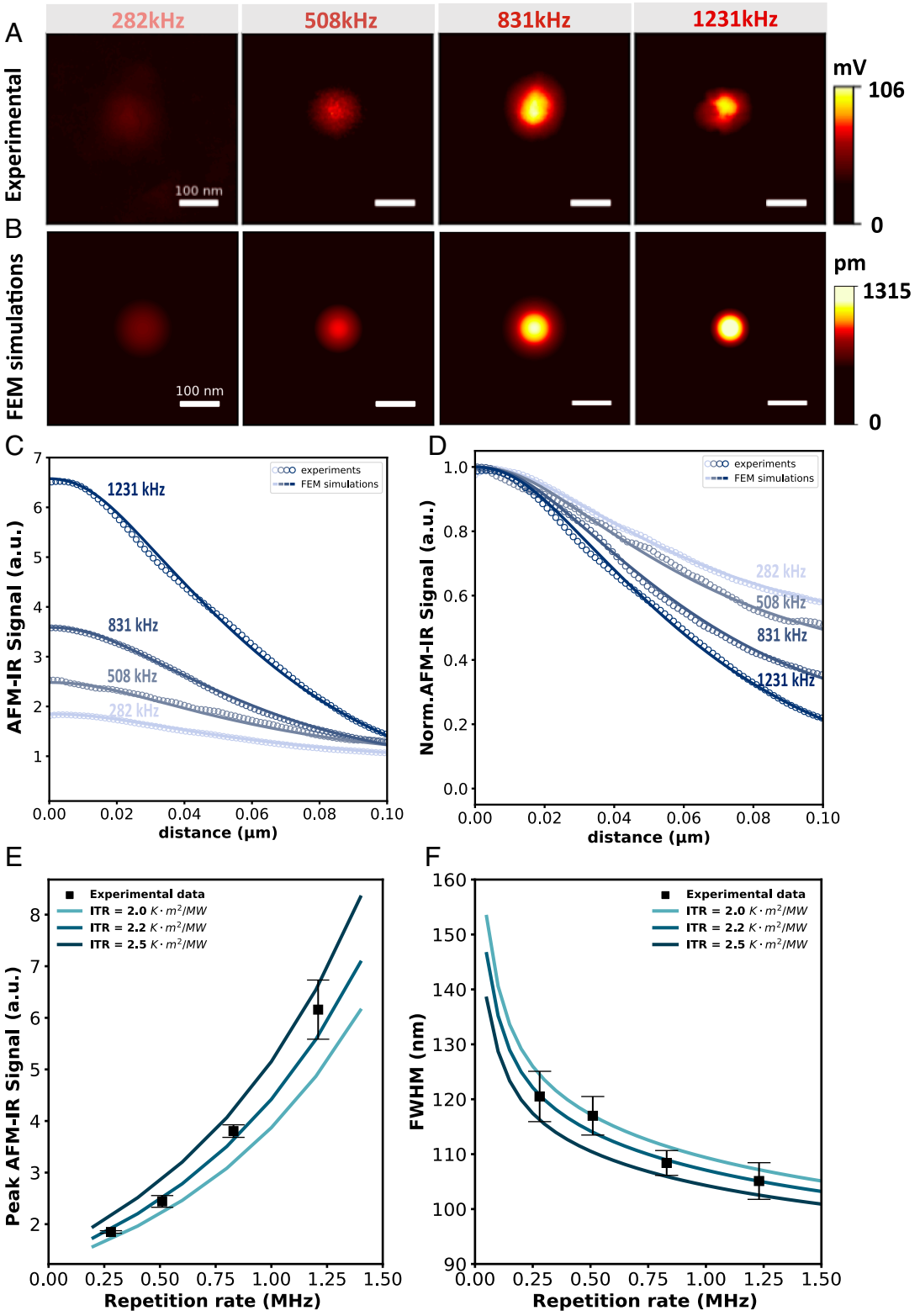

Fig. 5. AFM-IR images were obtained for various laser repetition rates. (*A*) Experimental AFM-IR images were obtained using a series of laser repetition rates at a pulse width of 100 ns. (*B*) Simulated AFM-IR images under the same experimental parameters. Considering a peak laser power of 4.5 mW, beam diameter r_{laser} = 10 μm, diameter of 140 nm for the absorber, positioned at a depth of 0.93 μm, tightly under the surface. (*C*) The AFM-IR signal at each examined frequency is scaled to a baseline value, with solid lines representing the FEM simulations at each corresponding frequency. (*D*) The AFM-IR signal at each examined frequency is normalized to its local peak value, with solid lines representing the FEM simulations at each corresponding frequency. (*E*) Peak amplitudes of AFM-IR signal in dependence on laser repetition rates. The simulated line represents the trend of the peak surface displacement based on FEM simulations. (*F*) FWHM of AFM-IR signal cross-section was measured at laser repetition rates of 282 kHz, 508 kHz, 831 kHz, and 1,231 kHz. The reported measurements include the mean value as well as the maximum deviation from repeated measurements. The FEM simulated line represents the trend of the FWHM as a function of laser repetition rates. The simulation presented in *SI Appendix*, Fig. S7 is based on the PSF model and does not include consideration for the thermal resistance at the interface.

The model and experiment both show an increasing peak amplitude at constant pulse width and increasing repetition rate (Fig. 5 *C* and *E*). The increasing peak amplitude can be attributed to the increasing duty cycle and thus increasing energy deposited in the absorber. The peak amplitude at the highest tested frequency (1,231 kHz) deviates from the trend seen for the other frequency but follows the FWHM trend (*SI Appendix*, Fig. S20 and Fig. 5*F*). This is due to the fact that at this setting a duty cycle of 12.3% had been reached which goes beyond the specifications of the laser used. In this regime the external cavity quantum cascade lasers (EC-QCLs) control circuit will skip every other pulse so as to stay within the maximum duty cycle specifications of the device and avoid damage, leading to a 50% reduction in peak amplitude. The FWHM is not affected by this.

We use the FWHM of the AFM-IR signal distribution profile, as depicted in Fig. 5*F* to determine the achievable spatial resolution. Experiments and models agree that increasing the laser repetition rates led to a decrease in FWHM, indicating improved spatial resolution (Fig. 5*D*). In the following section, we show that this effect can be understood through the PSF model.

The model and simulation also agree well when it comes to the effect of pulse width. When keeping the repetition rate around 282 kHz and varying the pulse width from 100 ns to 500 ns at constant peak pulse power, a linear dependence of peak and integrated amplitude on the pulse width is found (Fig. 6). To compare modeled and measured amplitude a scaling factor is required, as the models directly output surface displacement,

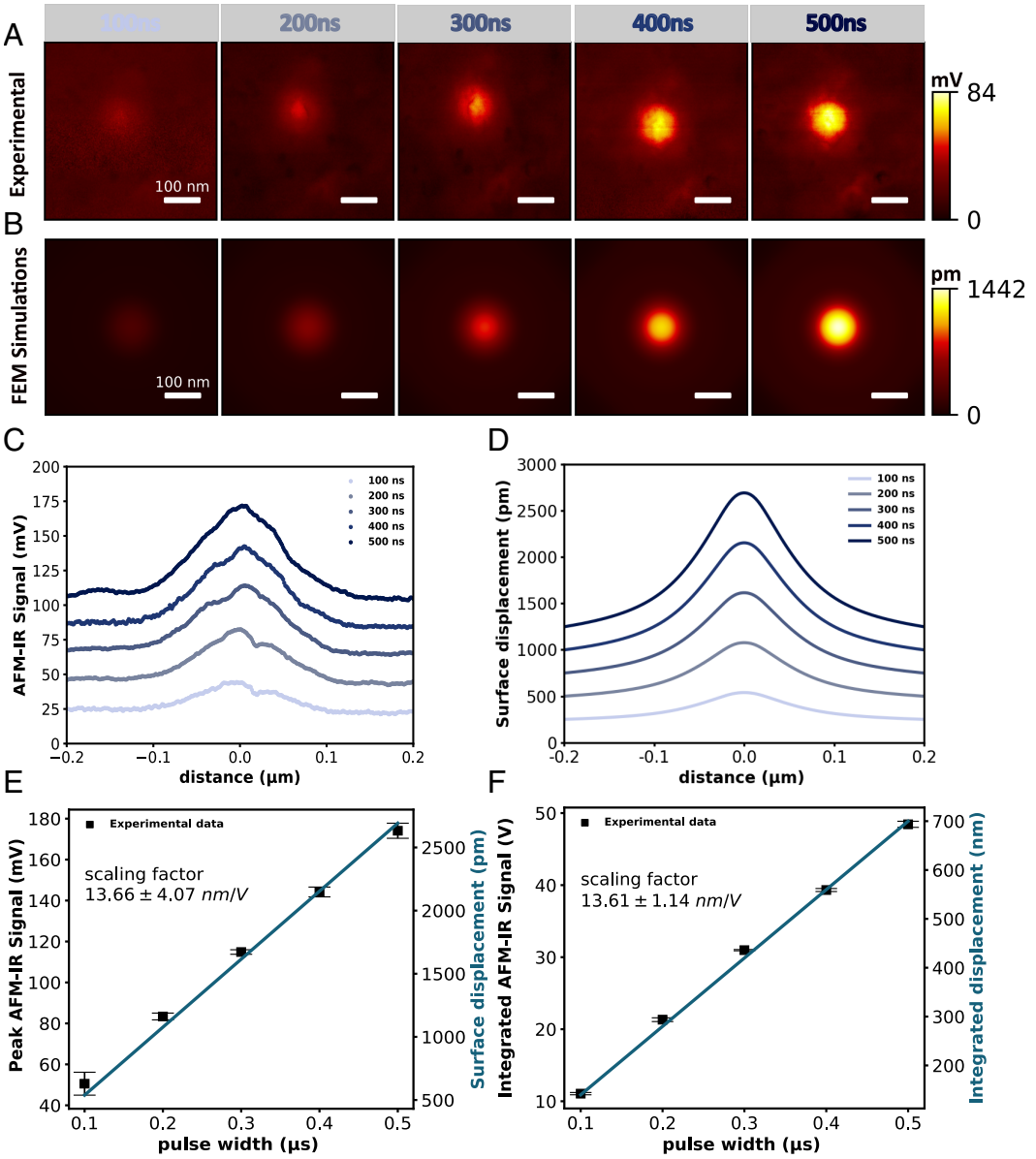

Fig. 6. AFM-IR signal dependence on pulse width. (*A*) Experimental AFM-IR images were obtained using a series of laser pulse widths ranging from 100 ns to 500 ns at a laser repetition rate of 282 kHz. To highlight the distinct contrast between the figures acquired at different frequencies, all images were subtracted by their respective minimum values. The figures displaying the original minimum values are presented in *SI Appendix*, Fig. S8. (*B*) Simulated AFM-IR images under the same experimental parameters. Considering laser power 4.5 mW, a diameter of 100 nm for the absorber, positioned at a depth of 0.93 µm. (*C*) The experimental AFM-IR signal profile over axial displacement measured at different pulse widths. (*D*) FEM simulation of surface displacement profiles at different pulse widths. (*E*) Peak AFM-IR signal and simulated peak surface displacement in dependence on pulse widths. The reported measurements represent the mean values with the maximum deviation from repeated measurements. (*F*) Integrated AFM-IR signal and simulated integrated surface displacement over the radial coordinate from −2 µm to 2 µm depending on pulse widths.

while the AFM-IR signal is proportional to surface displacement but has several sensitivity constants that are difficult to determine (17). We have determined a scaling factor of 13.61 ± 1.14 nm/V as described in *Materials and Methods* to show that the linear relation seen in the simulation is matched by the behavior in the experiment. However, it should be noted that this factor only relates experimental AFM-IR signal amplitude to simulated surface displacement. The actual experimental surface displacement is thus proportional to the simulated one but not equal to it, as this factor depends on the type of cantilever, the AFM instrument, the resonance mode, laser power, and laser profile on the surface.

This effect, too, is due to the increasing duty cycle and thus increasing energy deposited in the absorber. This effect is not true for arbitrary long pulse widths, as will be discussed below.

Effects of Experimental Parameters on the AFM-IR Signal. Having established that the PSF and FEM model and FEM model and experiment, respectively, agree well, we can now leverage the analytical description of the PSF model to understand the effects of experimental parameters on the AFM-IR signal.

As the PSF model can describe the signal of a three-dimensional absorber, in addition to time/frequency domain behavior (9) it can also describe the lateral extension of the deflection caused by an absorber, which allows to determine the spatial resolution of the AFM-IR measurement. In general, modes with higher β_m will lead to a narrower profile due to the only r dependent term $J_0(\beta_m r)$ in Eq. **8**. These narrower modes will have a faster decay in time as λ_{mn} increases with m affecting the time-dependent term $\mathcal{T}_{nm}(t)$ defined in Eq. **7**.

Thus, resonance enhanced AFM-IR at higher frequencies and other AFM-IR techniques that use high frequencies by default, such as tapping mode AFM-IR and surface-sensitive AFM-IR, provide a better lateral spatial resolution.

The PSF model also shows a relationship between the FWHM of the surface displacement and the distance $h_{\mathrm{mat}} - z_0$ of the absorber from the surface. The further the absorber is from the surface the wider the FWHM (Fig. 7*A*). This behavior can be explained by looking at the z_0 dependence of $A(\beta_m, \eta_n)$. For a spherical absorber this can be easiest explained through the following part of $A(\beta_m, \eta_n)\sin(\eta_n z_0)\sin(\eta_n R_{\mathrm{abs}})$ (Eq. **10**). This expression will always be positive for low z_0 but for $z_0 \approx h_{\mathrm{mat}}$ will be positive for even n be positive and for odd n be negative. As the mode shape in $r \propto J_0(\beta_m r)$ this means that for absorbers close to the surface the wider lower-order modes in m for $n = 0$ are counteracted by negative contributions from $n > 0$. The $\sin(\eta_n z_0)\sin(\eta_n R_{\mathrm{abs}})$ term also explains the higher surface displacement for absorbers close to the surface: At $z_0 \propto 0$, $\sin(\eta_n z_0)$ will also be close to zero.

Taking a closer look at the frequency dependence of the spatial resolution, Eq. **7** allows us to understand the effect of pulse width on the achievable spatial resolution. For a rectangular pulse $\prod\left(\frac{t}{t_p}\right)$ (e.g. in the case of an EC-QCL), in the frequency domain

$$\mathcal{T}_{nm}(f) = \frac{2\alpha\lambda_{mn}^2}{\alpha^2\lambda_{mn}^4 + 4\pi^2 f^2} \cdot t_p \,\mathrm{sinc}\left(t_p f\right) \qquad [11]$$

For a pulse train of repetition rate f_{rep}, the above expression is multiplied by a Dirac comb

$$f_{\mathrm{rep}} \sum_{k=-\infty}^{\infty} \delta\left(f - k f_{\mathrm{rep}}\right) \qquad [12]$$

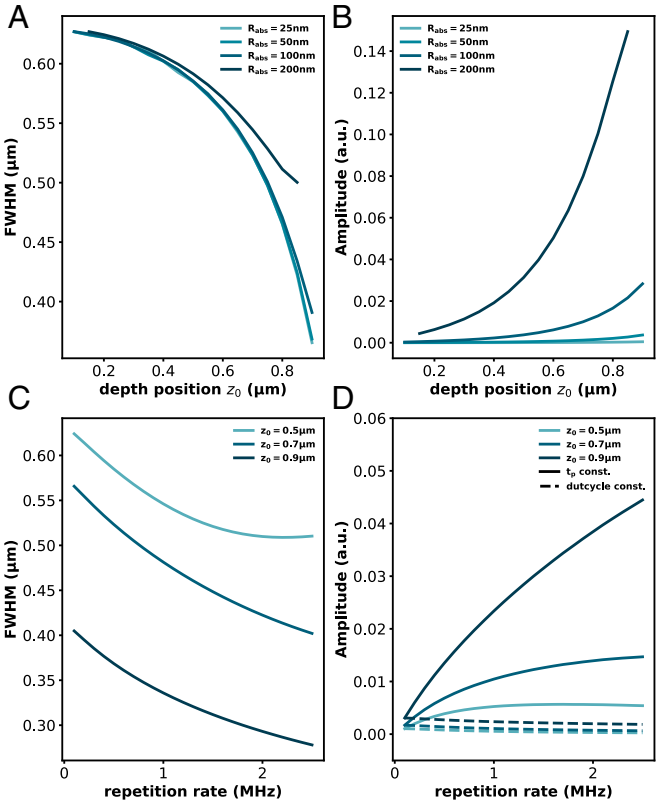

Fig. 7. FWHM and amplitude exhibit dependencies on the position of absorber depths and laser repetition rates. (*A*) FWHM and (*B*) amplitude are examined at various absorber depth positions for four different absorber sizes. The laser pulse has a duration of 100 ns, and the repetition rate is 500 kHz. (*C*) FWHM and (*D*) amplitude are examined at different laser repetition rates for three distinct absorber depth positions. Solid lines represent simulations at a constant laser pulse duration of 100 ns, and dash lines represent simulations with a constant duty cycle of 1%. The absorber has a radius of 50 nm.

with δ being Dirac's delta. In this case, typically the signal is demodulated at f_{rep} or one of its multiples.

Thus, when the laser is pulsed at a fixed frequency, the Fourier transformed $\prod$ merely acts as a scaling factor that affects all $A(\beta_m, \eta_n)$ in the same way. Pulse width thus only affects the signal amplitude but not the spatial resolution. We can also see that the pulse width does affect overall signal amplitude. It reaches a maximum at $t_p = \frac{1}{2f}$ and then decreases back down to 0 at $t_p = \frac{1}{f}$. Note that f here is not necessarily the laser repetition rate f_{rep} but the frequency at which the signal is demodulated. Hence, when demodulating the AFM-IR signal at a multiple of the laser repetition rate (as is sometimes done to reach cantilever resonances beyond the maximum pulse repetition rate of the laser) care has to be taken, that the product of the demodulation frequency and pulse width $ft_p \leq 0.5$ (see the relationship between laser amplitude and duty cycle in Fig. 8). Increasing $ft_p > 0.5$ does not increase the amplitude of the signal and only leads to unnecessary sample heating. (Illustrations of the relationship between pulse width, signal amplitude, and frequency can be found in *SI Appendix*, Fig. S5). Even though the highest signal is achieved at 50% duty cycler, there is a good reason to keep the pulse width as short as possible when exciting the cantilever with a train of pulses: sample heating. While at constant peak pulse power the maximum signal amplitude is achieved at 50% duty cycle, when instead keeping the average power constant, the signal at duty cycles below 10% is more than 1.5 times higher than that at 50% (*SI Appendix*, Fig. S5*E*).

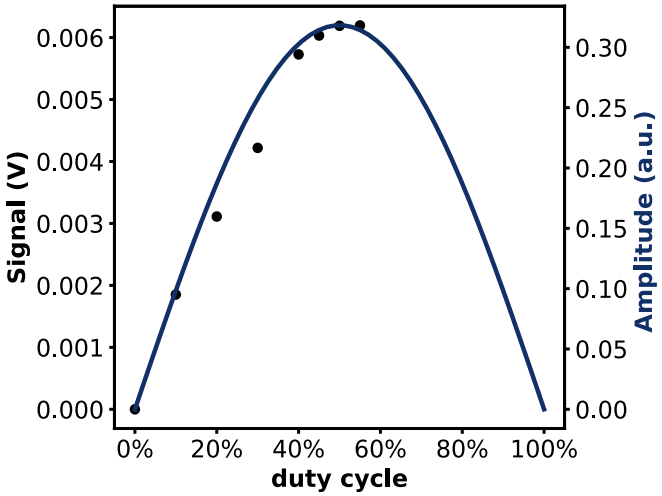

Fig. 8. The measured laser power and calculated signal amplitude as a function of duty cycle.

Consideration of cantilever dynamics, including mode analysis and beam slope, becomes crucial when higher resonances of the cantilever are excited (40). The contributions from the cantilever act as a transfer function to the final detected signal, as detailed in the original work by Dazzi et al. (17). *SI Appendix*, Fig. S17 illustrates the product of the calculated beam slope and the simulated surface displacement. It plots the peak value at each mode frequency, demonstrating a good agreement with the experiments. More details can be found in *SI Appendix*.

As mentioned above, increasing the pulse repetition rate will narrow the FWHM of the surface displacement (i.e. improve spatial resolution). However, this does not affect absorbers at all depths in the same way (Fig. 7*C*). Here, for absorbers buried deeper below the surface a "leveling out" effect can be seen, whereby further increase of the repetition rate does not improve the spatial resolution.

Finally, the PSF model also helps to explain the depth resolution of the surface-sensitive AFM-IR (Fig. 7*D*). At constant pulse width, the peak amplitude caused by an absorber buried deeper inside the sample plateaus at lower frequencies than that of those closer to the surface (continuous lines). When the experiment is conducted at constant duty cycle, this appears as an overall decrease of the peak amplitude of the buried absorber compared to that of absorbers closer to the surface (dashed lines).

Conclusions

This work establishes an analytical expression that describes the surface displacement caused by a three-dimensional absorber embedded within a matrix in an AFM-IR experiment. This point spread function model provides a detailed understanding of the photothermal expansion and AFM-IR signal generation processes. Based on this model we can understand the effect of experimental parameters and sample geometry on signal amplitude and spatial resolution.

The PSF model was rigorously validated through comparisons with FEM simulations and experimental data.

The developed PSF model explains that increasing the pulse width enhances the signal as long as the product of pulse width and demodulation frequency is kept below 0.5. Furthermore, our experimental data agree with the PSF model, which also does not find a direct relation between pulse width and spatial resolution, aligning with the findings of other researchers (20).

The demodulation frequency is found to be the main factor under the control of the AFM-IR user for a given sample and cantilever that affects spatial resolution. Higher frequency improves resolution. At constant pulse width it also increases peak amplitude.

The PSF model can also be used to study vertical resolution of high-frequency AFM-IR modes, showing that the peak signal amplitude from absorber far from the surface will decay with increasing demodulation frequency.

In comparing experimental data and FEM model, we have identified the interfacial thermal resistance between phases as a significant contribution to the AFM-IR signal. While the determination of interfacial thermal resistance in AFM-IR using custom transducers has previously been demonstrated (7, 41), specialized, high-frequency AFM-IR tips were demonstrated for the determination of this often elusive parameter, our results hint at an alternative approach that leverages the frequency-dependent AFM-IR image combined with modeling. In this work, the interfacial thermal resistance between PMMA absorber and PE $R_{PMMA/PE}$ was found to be $\approx 2.2 \times 10^{-6}$ m^{-2} KW^{-1}.

The combination of optical and photoelastic effects in AFM-IR also need to be taken into account when evaluating spectra, as peak amplitude caused by an absorber not only depend on its vertical but also its lateral extension.

Our study confirms the following properties of the AFM-IR signal that have also been found in previous work that did not model an inhomogeneous sample:

1. The AFM-IR signal linearly depends on the coefficient of thermal expansion α_z.
2. Higher modulation frequencies/pulse rates lead to higher spatial resolution.
3. The spatial resolution in AFM-IR remains independent of the pulse width/duty cycle of the laser (see point 10 for limits).
4. In small spherical absorbers it is the volume rather than the height that is proportional to the AFM-IR signal—this remains true even for buried spheres.
5. High thermal conductivity of the matrix reduces the signal amplitude and degrades spatial resolution.

Beyond confirming these established properties of the AFM-IR signal our study also allows us to deduce the following relationships:

6. With increasing depth (distance from the surface) the apparent size of absorbers increases.
7. The spatial resolution of AFM-IR remains independent of Young's modulus, Poisson's ratio, and the thermal expansion coefficient.
8. The AFM-IR signal amplitude decreases for absorbers located deeper within the sample.
9. Modulation at higher frequencies preferentially generates signal from absorbers closer to the surface.
10. When exciting with a pulse train, the signal at duty cycle $<10\%$ is more than 1.5 times higher than that at 50% at the same average power.

While our model does not take into account acoustic waves, Chae et al. reported the detection of such waves in the air in an AFM-IR experiment using a nanophotonic transducer (7), and Raschke et al. studied them in the context of photoinduced force experiments (42). Despite regarding the acoustic wave as negligible in our current study, investigating the coupling of photothermal and photoacoustic effects would constitute a valuable addition and could potentially contribute to a better

understanding of how to either use these phenomena to gain additional insight into the sample or better understand how to remove their contribution to the AFM-IR signal.

Furthermore, assumptions underlying this model preclude its direct application to some interesting sample configurations that have been analyzed with AFM-IR. For example, in the graphene on SiO_2 substrate sample analyzed by Menges et al. (43) it is not the sample layer or the graphene absorber that produces the thermal expansion required for AFM-IR but the SiO_2 substrate. Likewise, substrates with low thermal conductivity in comparison to that of the sample (44) or high coefficient of thermal expansion will require a modification of the model. In such cases verification of the validity of the assumptions underlying the Green's function approach using FEM is prudent. The comparison between experimental data and FEM model also demonstrates the importance of interfacial thermal resistance on the AFM-IR signal amplitude and spatial resolution. This point should be taken into account when studying interfaces.

The developed PSF model of AFM-IR provides researchers with a powerful tool for quantitative analysis and optimization of nanoscale chemical imaging experiments. Beyond the applications and results shown in this work, a conversion to Cartesian coordinates can be envisioned. This would allow to study more complex samples. As the PSF model is significantly more efficient than a comparable FEM approach it can provide deeper insights into advanced, nonlinear AFM-IR techniques, such as surface-sensitive AFM-IR. Potentially, the model could also be used to combine AFM-IR images taken at different frequencies to perform tomography to determine the vertical makeup of a sample.

Materials and Methods

Sample Preparation. The PE/PMMA sample was prepared by melting and mixing a PE matrix (average Mw 35.000, Sigma Aldrich) just above the melting temperature (Tm = 116 °C) while keeping in motion through vigorous stirring and subsequently adding nano-beads of poly(methyl methacrylate) (PMMA, Tm = 160 °C) with average diameter 140 nm (PolyAn Pink, PolyAn GmbH). The beads are dispersed in a water solution with a solid content of 1% and were pipetted onto the molten PE. This evaporates the water but does not melt PMMA. Stirring was continued until beads were thoroughly mixed into the PE. Then the mixture was cooled to room temperature. For further drying, the sample was placed into an oven (105 °C) for 3 h.

The sample was ultracryomicrotomed to a thickness of 1 μm and placed on Si substrates for measurements.

AFM-IR Experimental and Data Collection. All AFM-IR data were collected using a nanoIR3s (Bruker) controlled by Analysis Studio (Anasys Instruments, v3.15).

Experiments were conducted using an overall gold coated contact mode cantilever (Cont-GB-C, BudgetSensors Innovative Solutions Bulgaria Ltd.) with a nominal first resonance frequency of 13 ± 4 kHz and a nominal spring constant between 0.04 N m^{-1} and 0.40 N m^{-1}. As source for photothermal excitation, a mid-IR EC-QCL (MIRcat-QT, DRS Daylight Solutions Inc.) was used. All AFM-IR measurements were performed in resonance enhanced contact mode AFM-IR. For AFM-IR images a 500 nm × 500 nm area was scanned with a line rate of 0.1 Hz (lateral speed 100 nm s^{-1}) and a resolution of 400 pixels per line at 200 lines. For chemical imaging the distinct carbonyl-stretching band of PMMA (C=O) at 1,730 cm^{-1} was selected and pulse peak power was set as 15 mW. The polarization of the laser source is set to 0 degrees in respect to the sample plane. The laser repetition rate was kept at the frequency of the contact resonance of the cantilever using a phase-locked loop (PLL).

The experiments were performed at a series of laser pulse widths of 100 ns, 200 ns, 300 ns, 400 ns, and 500 ns each at laser repetition rates of 282 kHz, 508 kHz, 831 kHz, and 1,231 kHz. For each laser pulse width and repetition rate setting, three IR images were collected. Simultaneously with the IR images (trace and retrace), also height images (trace and retrace), deflection channel (trace and retrace), and the PLL frequency channel (trace and retrace) were recorded.

The AFM-IR instrument and laser beam paths were encased and purged with dry air.

Scaling Factor Determination. The original figures of Figs. 5 and 6 with the their respective minimum values are presented in *SI Appendix*, Figs. S6 and S8. Fig. 5 *C* and *D* illustrate the cross-section through the chemical images and FEM simulations at different pulse widths from Fig. 5 *A* and *B*. In the absence of consideration for the interfacial thermal resistance between PMMA beads and PE, the simulated surface displacement profiles exhibit much greater width compared to the cross-section profiles observed in the experiments, as depicted in *SI Appendix*, Fig. S9.

Fig. 6 *E* and *F* depict that the simulated peak and integrated surface displacement exhibit a linear growth trend with the pulse width. When compared with the experimental results, scaling factors (accounting for a range of experimental sensitivity factors) of 13.66 ± 4.07 nm/V and 13.61 ± 1.14 nm/V were obtained for the surface displacement and the AFM-IR signal, respectively, by calculating the mean ratio of the deflection signal amplitude and the model surface deformation. Calculated scaling factors for the surface displacement and the AFM-IR signal at each pulse width are shown on *SI Appendix*, Fig. S10.

Laser Power Duty Cycle Measurement. A custom EC-ICL (ALPES Lasers SA) was used to probe the behavior of the AFM-IR signal at high duty cycle (Fig. 8). The device emits between 2,800 cm^{-1} to 3,100 cm^{-1} and achieves pulse widths of up to 3,000 ns at repetition rates up to 180 kHz at >10 mW peak power and up to 100% duty cycle.

Data, Materials, and Software Availability. Docker container with raw data and code for data evaluation have been deposited in Zenodo (DOI: 10.5281/zenodo.10518024) (45).

ACKNOWLEDGMENTS. This work was funded with financial support from the European Union's Horizon 2020 research and innovation programme. Y.Z., L.O., G.R., and B.L. acknowledge the Marie Skłodowska-Curie project "Optical Sensing using Advanced Photo-Induced Effects" under grant agreement No. 860808. U.Y. and G.R. acknowledge the European Commissions's Horizon 2020 project "High-Performance Large Area Organic Perovskite devices for lighting, energy and Pervasive Communication" under grant agreement No. 861985. G.R. also acknowledges support from European Commissions's Horizon 2020 project "Tumor and Lymph Node on Chip for cancer studies" under grant agreement number 953234. G.V.B.L. acknowledges support from Conselho Nacional de Desenvolvimento Científico e Tecnológico under grant agreement No. 307415/2022-8. The financial support by the Austrian Federal Ministry for Labour and Economy and the National Foundation for Research, Technology and Development and the Christian Doppler Research Association is gratefully acknowledged. We would like to thank Andrew Cashman for his valuable input and the discussions. Furthermore, we would also like to thank Jakob Gruber and Karin Whitmore for microtoming some samples using facilities at the University Service Centre for Transmission Electron Microscopy, Technische Universität Wien. We would also like to thank Dr. Andrea Centrone for pointing out a mistake in the preprint.

Author affiliations: [a]Faculty of Technical Chemistry, Institute of Chemical Technologies and Analytics, Technische Universität Wien, Vienna 1060, Austria; [b]Physics Department, Centre for Advanced Photonics and Process Analysis, Munster Technological University, Cork T12P928, Ireland; [c]Department of Physics, Universidade Tecnológica Federal do Paraná, Medianeira PR 85884-000, Brazil; and [d]Faculty of Technical Chemistry, Christian Doppler Laboratory for Advanced Mid-Infrared Laser Spectroscopy in (Bio-)Process Analytics, Technische Universität Wien, Vienna 1060, Austria

1. A. Centrone, Infrared imaging and spectroscopy beyond the diffraction limit. *Annu. Rev. Anal. Chem.* **8**, 101–126 (2015).
2. A. Dazzi, C. B. Prater, AFM-IR: Technology and applications in nanoscale infrared spectroscopy and chemical imaging. *Chem. Rev.* **117**, 5146–5173 (2017).
3. A. M. Katzenmeyer *et al*., Mid-infrared spectroscopy beyond the diffraction limit via direct measurement of the photothermal effect. *Nanoscale* **7**, 17637–17641 (2015).
4. A. Dazzi *et al*., AFM-IR: Combining atomic force microscopy and infrared spectroscopy for nanoscale chemical characterization. *Appl. Spectrosc.* **66**, 1365–1384 (2012).
5. A. C. V. dos Santos, B. Lendl, G. Ramer, Systematic analysis and nanoscale chemical imaging of polymers using photothermal-induced resonance (AFM-IR) infrared spectroscopy. *Polym. Test.* **106**, 107443 (2022).
6. F. S. Ruggeri, B. Mannini, R. Schmid, M. Vendruscolo, T. P. J. Knowles, Single molecule secondary structure determination of proteins through infrared absorption nanospectroscopy. *Nat. Commun.* **11**, 2945 (2020).
7. J. Chae *et al*., Nanophotonic atomic force microscope transducers enable chemical composition and thermal conductivity measurements at the nanoscale. *Nano Lett.* **17**, 5587–5594 (2017).
8. G. Ramer, V. A. Aksyuk, A. Centrone, Quantitative chemical analysis at the nanoscale using the PTIR technique. *Anal. Chem.* **89**, 13524–13531 (2017).
9. J. J. Schwartz, D. S. Jakob, A. Centrone, A guide to nanoscale IR spectroscopy: Resonance enhanced transduction in contact and tapping mode AFM-IR. *Chem. Soc. Rev.* **51**, 5248–5267 (2022).
10. F. Lu, M. Jin, M. A. Belkin, Tip-enhanced infrared nanospectroscopy via molecular expansion force detection. *Nat. Photon.* **8**, 307–312 (2014).
11. A. V. D. dos Santos, D. Tranchida, B. Lendl, G. Ramer, Nanoscale chemical characterization of a post-consumer recycled polyolefin blend using tapping mode AFM-IR. *Analyst* **147**, 3741–3747 (2022).
12. F. Tang, P. Bao, Z. Su, Analysis of nanodomain composition in high-impact polypropylene by atomic force microscopy-infrared. *Anal. Chem.* **88**, 4926–4930 (2016).
13. L. Baldassarre *et al*., Mapping the amide I absorption in single bacteria and mammalian cells with resonant infrared nanospectroscopy. *Nanotechnology* **27**, 075101 (2016).
14. A. Dazzi *et al*., Chemical mapping of the distribution of viruses into infected bacteria with a photothermal method. *Ultramicroscopy* **108**, 635–641 (2008).
15. Y. Yuan *et al*., Photovoltaic switching mechanism in lateral structure hybrid perovskite solar cells. *Adv. Energy Mater.* **5**, 1500615 (2015).
16. J. Houel *et al*., Ultraweak-absorption microscopy of a single semiconductor quantum dot in the midinfrared range. *Phys. Rev. Lett.* **99**, 217404 (2007).
17. A. Dazzi, F. Glotin, R. Carminati, Theory of infrared nanospectroscopy by photothermal induced resonance. *J. Appl. Phys.* **107**, 124519 (2010).
18. A. Dazzi, "PhotoThermal induced resonance. Application to infrared spectromicroscopy" in *Thermal Nanosystems and Nanomaterials*, S. Volz, Ed. (Springer Berlin Heidelberg, Berlin, Heidelberg) (2009), vol. 118, pp. 469–503.
19. A. N. Morozovska *et al*., Photothermoelastic contrast in nanoscale infrared spectroscopy. *Appl. Phys. Lett.* **112**, 033105 (2018).
20. J. J. Schwartz, G. Pavlidis, A. Centrone, Understanding cantilever transduction efficiency and spatial resolution in nanoscale infrared microscopy. *Anal. Chem.* **94**, 13126–13135 (2022).
21. B. Lahiri, G. Holland, A. Centrone, Chemical imaging beyond the diffraction limit: Experimental validation of the PTIR technique. *Small* **9**, 439–445 (2013).
22. L. Quaroni, Understanding and controlling spatial resolution, sensitivity, and surface selectivity in resonant-mode photothermal-induced resonance spectroscopy. *Anal. Chem.* **92**, 3544–3554 (2020).
23. A. V. D. dos Santos *et al*., Nanoscale infrared spectroscopy and chemometrics enable detection of intracellular protein distribution. *Anal. Chem.* **92**, 15719–15725 (2020).
24. X. Ma *et al*., Nanoscale IR spectroscopy: From principles to nanoscale imaging and identification of metal soaps. *Microsc. Microanal.* **27**, 2814–2815 (2021).
25. S. Kenkel *et al*., Chemical imaging of cellular ultrastructure by null-deflection infrared spectroscopic measurements. *Proc. Natl. Acad. Sci. U.S.A.* **119**, e2210516119 (2022).
26. F. Bai, R. Bertram, B. R. Karamched, A closed-loop multi-scale model for intrinsic frequency-dependent regulation of axonal growth. *Math. Biosci.* **344**, 108768 (2022).
27. S. Kenkel, S. Mittal, R. Bhargava, Closed-loop atomic force microscopy-infrared spectroscopic imaging for nanoscale molecular characterization. *Nat. Commun.* **11**, 3225 (2020).
28. J. Mathurin, A. Deniset-Besseau, A. Dazzi, Advanced infrared nanospectroscopy using photothermal induced resonance technique, AFMIR: New approach using tapping mode. *Acta Phys. Pol. A* **137**, 29–32 (2020).
29. J. Mathurin *et al*., Photothermal AFM-IR spectroscopy and imaging: Status, challenges, and trends. *J. Appl. Phys.* **131**, 010901 (2022).
30. N. Noda, R. B. Hetnarski, Y. Tanigawa, *Thermal Stresses* (Taylor & Francis, New York, ed. 2, 2003).
31. G. Balasubramanian, I. K. Puri, Heat conduction across a solid-solid interface: Understanding nanoscale interfacial effects on thermal resistance. *Appl. Phys. Lett.* **99**, 013116 (2011).
32. K. D. Cole, Ed., "Series in computational and physical processes in mechanics and thermal sciences" in *Heat Conduction Using Green's Functions* (CRC Press, Boca Raton, ed. 2, 2011).
33. E. D. Black, I. S. Grudinin, S. R. Rao, K. G. Libbrecht, Enhanced photothermal displacement spectroscopy for thin-film characterization using a Fabry-Perot resonator. *J. Appl. Phys.* **95**, 7655–7659 (2004).
34. A. Dazzi, F. Glotin, R. Carminati, Theory of infrared nanospectroscopy by photothermal induced resonance. *J. Appl. Phys.* **107**, 124519 (2010).
35. P. E. Hopkins, Thermal transport across solid interfaces with nanoscale imperfections: Effects of roughness, disorder, dislocations, and bonding on thermal boundary conductance. *Int. Sch. Res. Notices*, https://doi.org/10.1155/2013/682586 (2013).
36. J. Song, Y. Zhang, Effect of an interface layer on thermal conductivity of polymer composites studied by the design of double-layered and triple-layered composites. *Int. J. Heat Mass Transf.* **141**, 1049–1055 (2019).
37. K. Zheng, J. Zhu, Y. M. Ma, D. W. Tang, F. S. Wang, Interfacial thermal resistance between high-density polyethylene (HDPE) and sapphire. *Chin. Phys. B* **23**, 107307 (2014).
38. M. D. Losego, L. Moh, K. A. Arpin, D. G. Cahill, P. V. Braun, Interfacial thermal conductance in spun-cast polymer films and polymer brushes. *Appl. Phys. Lett.* **97**, 011908 (2010).
39. K. Ruan, X. Shi, Y. Guo, J. Gu, Interfacial thermal resistance in thermally conductive polymer composites: A review. *Compos. Commun.* **22**, 100518 (2020).
40. U. Rabe, J. Turner, W. Arnold, Analysis of the high-frequency response of atomic force microscope cantilevers. *Appl. Phys. A* **66**, S277–S282 (1998).
41. M. Wang *et al*., High throughput nanoimaging of thermal conductivity and interfacial thermal conductance. *Nano Lett.* **22**, 4325–4332 (2022).
42. B. T. O'Callahan, J. Yan, F. Menges, E. A. Muller, M. B. Raschke, Photoinduced tip-sample forces for chemical nanoimaging and spectroscopy. *Nano Lett.* **18**, 5499–5505 (2018).
43. F. Menges *et al*., Substrate-enhanced photothermal nano-imaging of surface polaritons in monolayer graphene. *APL Photonics* **6**, 041301 (2021).
44. S. Rizevsky, K. Zhaliazka, T. Dou, M. Matveyenka, D. Kurouski, Characterization of substrates and surface-enhancement in atomic force microscopy infrared analysis of amyloid aggregates. *J. Phys. Chem. C* **126**, 4157–4162 (2022).
45. Y. Zhang *et al*., Understanding the resolution and sensitivity in photothermal nanoscale chemical imaging - a point spread function approach. Zenodo. https://doi.org/10.5281/zenodo.10518024. Deposited 16 January 2024.